

# Interturn Fault Diagnosis in Induction Motors Using the Pendulous Oscillation Phenomenon

Behrooz Mirafzal, *Student Member, IEEE*, Richard J. Povinelli, *Senior Member, IEEE*, and Nabeel A. O. Demerdash, *Fellow, IEEE*

**Abstract**—A robust interturn fault diagnostic approach based on the concept of magnetic field pendulous oscillation, which occurs in induction motors under faulty conditions, is introduced in this paper. This approach enables one to distinguish and classify an unbalanced voltage power supply and machine manufacturing/construction imperfections from an interturn fault. The experimental results for the two case studies of a set of 5-hp and 2-hp induction motors verify the validity of the proposed approach. Moreover, it can be concluded from the experimental results that if the circulating current level in the shorted loop increases beyond the phase current level, an interturn fault can be easily detected using the proposed approach even in the presence of the existence of motor manufacturing imperfection effects.

**Index Terms**—Broken-bar, condition monitoring, induction motor, interturn short circuit, stator fault, transient modeling.

## I. INTRODUCTION

EARLY stages of stator interturn faults may often have negligible effects on the machine performance, however such faults may rapidly lead to substantial interturn faults and subsequently catastrophic failures. Stator faults are caused by partial stator winding insulation failures. Such partial stator winding insulation failures may in turn be caused by one or more of the following causes: frequent machine overloading, coil vibration, transient voltage stress, and PWM inverter induced surges, particularly in the presence of substantial cable length between a motor and its drive, ambient stresses, and aging of the stator winding insulation [1]. Interturn faults lead to generated heat in the defective region of a winding which causes the fault to rapidly progress to more severe forms such as phase-to-phase and phase-to-ground faults. In industrial processes, where a machine is playing a key role as a prime-mover or energy conversion device, a sudden machine failure will likely result in an overall process failure. Moreover, a severe fault such as a phase-to-ground fault may lead to irreversible damage to the stator winding and core [1], [2]. In other words, early stage fault detection will enable orderly process shutdown, thereby avoiding expensive repairs and minimizing lost production time. Accordingly, it is worthwhile to detect stator interturn faults at an early stage to prevent further damage to the machine and involved systems.

Manuscript received November 16, 2004; revised February 11, 2005. This work was supported by the National Science Foundation under Grant ECS-0322974. Paper no. TEC-00322-2004.

The authors are with the Department of Electrical and Computer Engineering, Marquette University, Milwaukee, WI 53233 USA (e-mail: behrooz.mirafzal@mu.edu; richard.povinelli@mu.edu; nabeel.demerdash@mu.edu).

Digital Object Identifier 10.1109/TEC.2005.853767

An induction machine with a healthy stator winding can be represented as a symmetrical three-phase circuit. Although a broken bar fault or dynamic eccentricity fault affects the stator phase currents, the machine can still be modeled as a symmetrical three-phase circuit since all three stator phases are affected identically by such a defect in a 120° sequenced manner. However, this is not the case for interturn short circuits occurring in one or more of the phases in the stator winding. Hence, an induction machine with a stator interturn fault is represented as an unsymmetrical three-phase system. It is well-known in power systems that an unsymmetrical three-phase system (circuit) can be modeled as a combination of three symmetrical systems, namely the positive, negative, and zero sequences [3]. Most investigations for online interturn fault diagnosis of induction machines are conceptualized from this circuitry representation point of view. Investigators have attempted to detect such faults by means of calculating the negative sequence current [4], [5] and the negative and zero sequence impedances [6], [7].

In spite of an extensive motor fault diagnostics literature, motor fault diagnostics still constitute an open problem. The difficulty is mainly caused by mechanical load variations, power supply unbalances and manufacturing/construction imperfections within the machine itself. The purpose of this paper is to extend the concept of pendulous oscillation [8], [9] to interturn short circuit fault diagnosis, in the presence of inherent machine and power supply unbalances.

## II. MAGNETIC FIELD PENDULOUS OSCILLATION

Under ideal conditions, the magnetic fields of an induction machine rotate at synchronous speed. However, any asymmetry in the stator windings or rotor bars, which may be due to manufacturing imperfections or machine failure, disturbs the air-gap magnetic field causing the air-gap magnetic field to oscillate around its original synchronously rotating axis. Although, this oscillation may exist even for a healthy machine due to the machine structural imperfections, this oscillation will be significant and detectable in a case of internal failure in induction machines such as broken bar and interturn faults. This pendulous oscillation has been thoroughly discussed and experimentally demonstrated for broken bar faults in two previous papers [8], [9]. Hence, it can be mentioned that there exists mainly two motions for the resultant (air-gap) magnetic field in an induction machine: 1) rotation at synchronous speed, and 2) pendulous oscillation. It has been shown that the range of this pendulous oscillation progressively increases with the increase in the number of broken bars [8], [9]. It will be shown here that the range of this pendulous oscillation also progressively

increases in proportionality with the circulating loop current magnitude in the shorted coil. However, the pendulous oscillation caused by interturn shorts is different in its nature (shape) from the pendulous oscillation caused by broken bar faults, and this aspect is delineated in this paper.

### III. MOTOR FAULT DIAGNOSIS USING THE MAGNETIC FIELD PENDULOUS OSCILLATION PHENOMENON

In this section the different shapes of the pendulous oscillation phenomenon obtained from different fault scenarios are demonstrated in Figs. 1–4. These figures were obtained through an induction motor simulation based on the winding function method [10] in conjunction with line-to-line flux linkage state-space modeling of induction motors in the ABC frame [11]. For further detail see the Appendix. In Figs. 1–4, the angular phase shift between the space vectors of stator currents and voltages are plotted in a polar coordinate manner in which the radius indicates the absolute value of the real part of the space vector of the stator currents. Any point  $(r, \delta)$  in this polar plot is determined by the following expressions:

$$r(t) = \text{abs}(\text{Re}(\vec{i}_s(t))) \quad (1)$$

$$\delta(t) = \angle \vec{i}_s(t) - \angle \vec{v}_s(t) \quad (2)$$

where  $\vec{v}_s$  and  $\vec{i}_s$  are the space vectors of the stator terminal voltages and currents, respectively. It should be emphasized that the  $\vec{v}_s$  and  $\vec{i}_s$  are functions of time and they should not be confused with phasor quantities. Here, the  $\vec{v}_s$  and  $\vec{i}_s$  are defined as follows:

$$\vec{v}_s(t) = \frac{2}{3}(v_{ab}(t) + \alpha v_{bc}(t) + \alpha^2 v_{ca}(t)) \quad (3)$$

$$\vec{i}_s(t) = \frac{2}{3}((i_a(t) - i_b(t)) + \alpha(i_b(t) - i_c(t)) + \alpha^2(i_c(t) - i_a(t))) \quad (4)$$

where  $\alpha = \exp(j2\pi/3)$  is the space vector operator and  $v_{ab}$ ,  $v_{bc}$  and  $v_{ca}$  are the stator terminal line to line voltages, while  $i_a$ ,  $i_b$ , and  $i_c$  are the stator terminal line currents.

In order to setup a relationship between different types of faults, such as stator interturn and rotor broken bar fault scenarios, the following cases, illustrated in Figs. 1–4, are considered:

- healthy induction motor; see Fig. 1;
- induction motor with a typical broken bar fault; see Fig. 2;
- induction motor with a stator interturn fault; see Fig. 3;
- healthy induction motor energized by an unbalanced power supply; see Fig. 4.

As the simulation results show in Figs. 1–4, each condition generates a different shape of the trace of the  $\vec{r} = r \angle \delta$  vector, which can be used for fault diagnosis/classification purposes. The differences in these shapes can be explained based on the physics of each of the above-mentioned conditions. In order to obtain a better understanding of the differences, an analytical explanation is given below.

*Case (a):* A healthy induction motor energized by a three-phase balanced voltage power supply. The space vectors of the

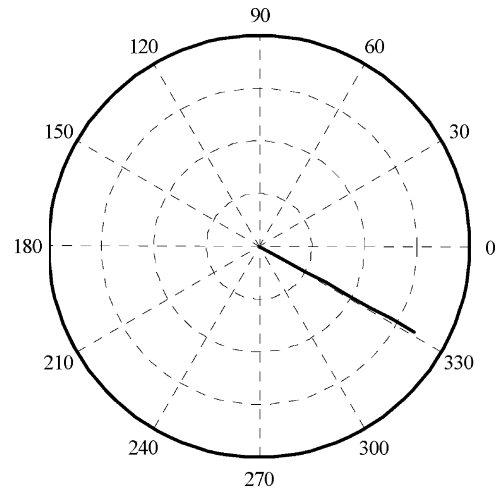


Fig. 1. Pendulous oscillation in a polar coordinate plot of  $r$  and  $\delta$  for a healthy induction motor, a straight line.

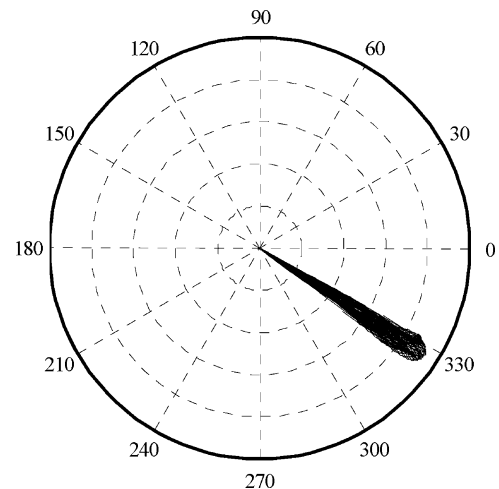


Fig. 2. Pendulous oscillation in a polar coordinate plot of  $r$  and  $\delta$  for an induction motor in case of a typical broken bar fault, a petal shape.

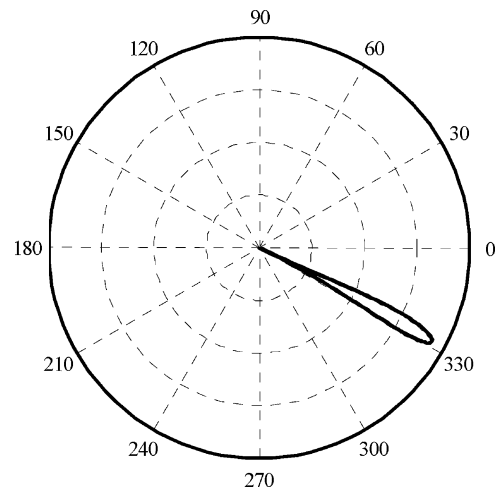


Fig. 3. Pendulous oscillation in a polar coordinate plot of  $r$  and  $\delta$  for an induction motor in case of interturn fault, an unfilled-petal shape.

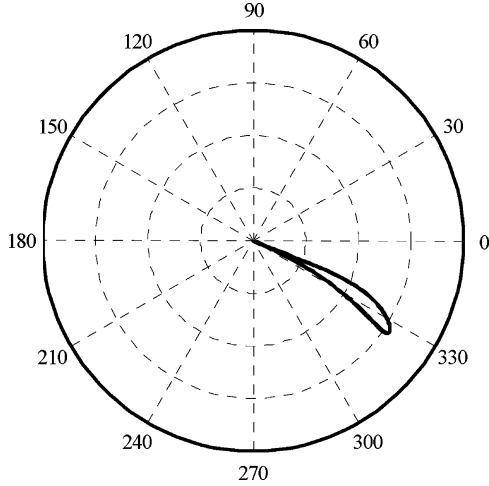


Fig. 4. Pendulous oscillation in a polar coordinate plot of  $r$  and  $\delta$  for a healthy induction motor energized by unbalanced power supply (in voltage amplitudes), an unfilled-concave-petal shape.

motor terminal voltages and currents are given as follows:

$$\vec{v}_s(t) = V_{Lm} \exp(j\omega t) \quad (5)$$

$$\vec{i}_s(t) = I_{Lm} \exp(j\omega t - \psi) \quad (6)$$

where  $V_{Lm}$  and  $I_{Lm}$  are the peak values of the voltage and current terms in (3) and (4),  $\omega$  is the supply frequency in electrical rad/sec, and  $\vec{v}_s$  as well as  $\vec{i}_s$  are the space vectors of the terminal voltages and currents defined in (3) and (4), respectively. Accordingly, in this case, one can write the following expressions for the  $r$  and  $\delta$  quantities:

$$r(t) = \text{abs}(I_{Lm} \cos(\omega t - \psi)) \quad (7)$$

$$\delta(t) = -\psi. \quad (8)$$

In other words, the polar plot of  $(r, \delta)$  is a straight (radial) line, as illustrated in Fig. 1.

*Case (b):* An induction motor with a typical rotor broken bars fault energized by a three-phase balanced voltage power supply. Accordingly, one can write the following expressions as approximations for the  $r$  and  $\delta$  quantities [8], [9], [12]:

$$r(t) = \text{abs}(I_{Lm}(t) \cos(\omega t - \psi)) \quad (9)$$

$$\delta(t) = -\psi - \frac{\Delta\delta}{2} \cos(2\omega_r t) \quad (10)$$

where the peak value of the current  $I_{Lm}(t)$  varies with time due to the existence of a broken bar fault,  $\Delta\delta$ , the so-called swing angle [9], is the peak-to-peak value of the pendulous oscillation, and  $\omega_r \ll \omega$  is the slip frequency's angular velocity. In other words, for any angle  $\delta$ , the  $r$  value is changing from zero to its maximum value. Therefore, in this case, the polar plot of  $(r, \delta)$  has a (filled) petal shape, as can be seen in Fig. 2, due to the fact that  $\omega_r \ll \omega$  in (9) and (10).

*Case (c):* An induction motor with a stator interturn fault energized by a three-phase balanced voltage power supply. In this case, the air-gap magnetic field can be resolved into two components which rotate at synchronous speed but in opposite directions. Also, the resultant (air-gap) magnetic field can be resolved into a main rotation at synchronous speed and an

oscillation around the main rotation, where the speed of this oscillation is twice the synchronous speed [12]. Accordingly, one can write the following expressions as approximations for the  $r$  and  $\delta$  quantities:

$$r(t) = \text{abs}(I_{Lm}(t) \cos(\omega t - \psi)) \quad (11)$$

$$\delta(t) = -\psi - \frac{\Delta\delta}{2} \cos(2\omega t). \quad (12)$$

Here, the speeds of variations of the  $r$  and  $\delta$  quantities with respect to time are the same, since the cosine expression in (11) is within the absolute value operator. In other words, at any angle  $\delta$ , the  $r$  quantity will not change from zero to its maximum value because  $r$  and  $\delta$  are varying with time simultaneously at the same rate. Therefore, in this case, the polar plot of  $(r, \delta)$  has an unfilled-petal shape, or in other words constitutes only the outer boundary of the petal shape, as can be seen in Fig. 3.

As one can observe from (10) and (12), the frequency of the pendulous oscillation due to an interturn fault  $2\omega$  is much larger than the frequency of the pendulous oscillation due to a broken bar fault,  $2\omega_r$  [13]. Hence, the frequency characteristic of the pendulous oscillation can be used in order to detect both faults even if they occur simultaneously.

*Case (d):* A healthy induction motor energized by an unbalanced three-phase voltage power supply. This case can be further categorized into two different cases [12].

- 1) High or low resistivity of one of the motor feeding phase lines. This will generate an unfilled-petal shape similar to Fig. 3 in Case (c). However, this similarity does not lead to ambiguities in fault diagnostics, since such unbalances will be detected in the measurement of the motor terminal voltages.
- 2) Unbalances in the power supply voltage amplitudes generate an unfilled-concave-petal shape, see Fig. 4.

Here in this paper, an interturn fault was modeled as a short circuit through a small resistor. This type of fault generates an unfilled-petal-like configuration with a slight degree of curvature in the shape. This will generate a shape similar to Fig. 4 of Case (d). However, this similarity, again, does not lead to ambiguities in fault diagnostics since any unbalances in the motor terminal voltages can be detected in the measurements at the motor terminals.

#### IV. EXPERIMENTAL RESULTS

A 5-hp, 6-pole, 460-V, and a 2-hp, 2-pole, 460-V set of induction motors were tested under interturn short circuit faults. The interturn short circuits were achieved through a 1- $\Omega$  resistor  $r_f$  for the 5-hp motor and a 0.8- $\Omega$  resistor for the 2-hp motor. The 5-hp motor was rewound such that there were twenty taps in one of the phases, while the 2-hp motor had only 5 taps. The stator winding connections of both motors are star (Y) connections, where the number of turns per phase for the 5-hp and the 2-hp motors were 240 and 216 turns, all in series, respectively. See Table I for further details. The 5-hp motor was also tested when it was energized by an unbalanced power supply. This was achieved through using a series resistor  $r_{se}$  in one of the motor phase feeding lines, as shown in the circuit schematic of Fig. 5.

TABLE I  
2-hp AND 5-hp INDUCTION MOTORS PROPERTIES

| Design Feature            | 2-hp Induction Motor | 5-hp Induction Motor |
|---------------------------|----------------------|----------------------|
| Power (hp)                | 2                    | 5                    |
| Voltage (V)               | 460                  | 460                  |
| Current (A)               | 2.7                  | 6.8                  |
| Speed (r/min)             | 3450                 | 1165                 |
| Number of Poles           | 2                    | 6                    |
| Number of coils per phase | 8                    | 6                    |
| Number of Turns per Phase | 216                  | 240                  |
| Type of Stator Windings   | Concentrated         | Lap                  |
| Number of Rotor Bars      | 36                   | 45                   |
| Number of Stator Slots    | 24                   | 36                   |

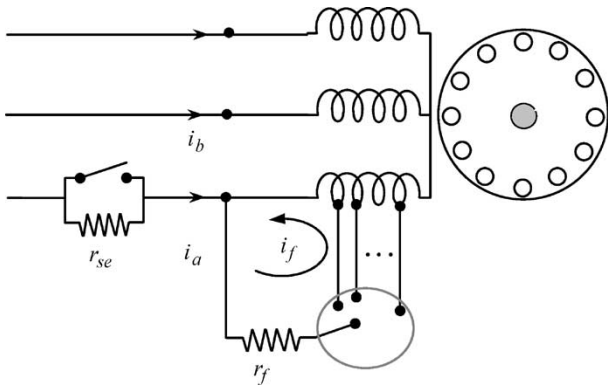


Fig. 5. Schematic representation of a tapped induction motor.

As representative examples of the many tests performed on the 2-hp and 5-hp induction motors in the laboratory, the pendulous oscillations of the 5-hp induction motor in a polar coordinate plot are shown in Figs. 6 and 7 with corresponding enlargements (zooms) in Figs. 8 and 9, respectively, for a healthy and a 12 turns (5%) fault. The short circuit was through a 1-Ω resistor,  $r_f = 1 \Omega$ . Again, the range of the pendulous oscillation, the so-called swing angle  $\Delta\delta$ , is shown for the above-mentioned cases of Figs. 6 and 7 in an enlarged fashion in Figs. 8 and 9, respectively. As one can see in Fig. 9, an interturn fault generates an unfilled-petal shape with a slight degree of curvature. This curvature is due to the existence of the resistor  $r_f$  in the circuit shown in Fig. 5, which is used to restrict the shorted loop current to an immune (safe) level of current that does not cause permanent coil damage. *The amplitude of the maximum thickness of the petal shape caused by the swing angle is used here as the interturn fault signature or index.*

The functional block diagram of an on-line interturn fault diagnosis using the swing angle,  $\Delta\delta$ , is depicted in Fig. 10. In this block diagram, the motor terminal currents and voltages are measured through current and voltage sensors and the outputs are digitized using an analog-to-digital (A/D) converter. The output signals of the A/D converter are filtered by a band pass filter (BPF), while the output signals of the BPF are further sampled (collected) throughout a period equal to the period of the power supply frequency; see Fig. 10. For each set of collected data

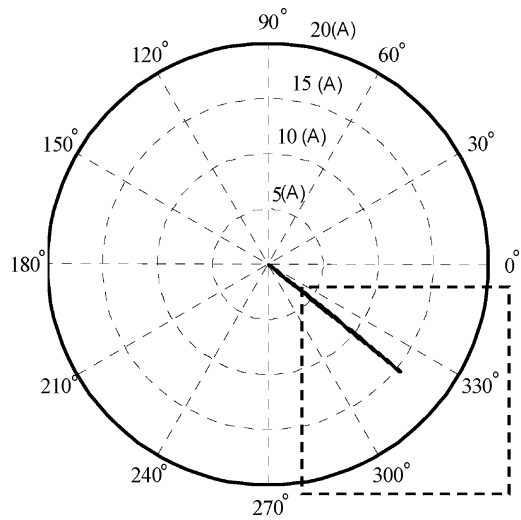


Fig. 6. Experimentally based results of the absolute value of  $Re(\vec{i}_s(t))$  in amperes versus angle  $\delta(t) = \angle \vec{i}_s(t) - \angle \vec{v}_s(t)$  in degrees for the case of the 5-hp induction motor under a healthy condition.

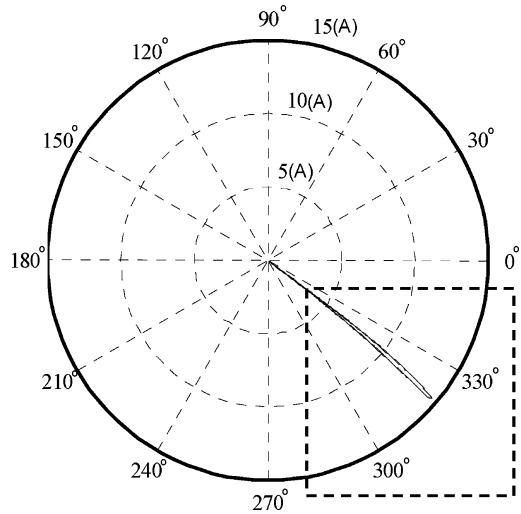


Fig. 7. Experimentally based results of the absolute value of  $Re(\vec{i}_s(t))$  in amperes versus angle  $\delta(t) = \angle \vec{i}_s(t) - \angle \vec{v}_s(t)$  in degrees for the case of the 5-hp induction motor under a faulty condition having 12 (5%) shorted turns, (shorted through 1-Ω resistor.)

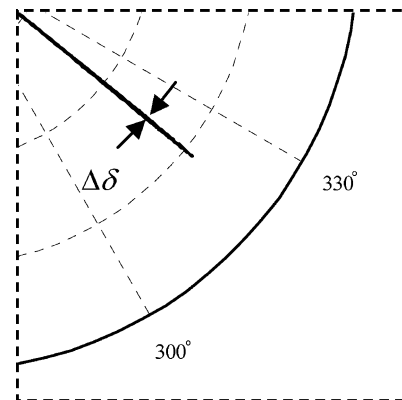


Fig. 8. Enlarged dotted-frame portion of Fig. 6, showing swing angle,  $\Delta\delta = \max(\Delta\delta(r) = \delta^{\max} - \delta^{\min})$ , in the healthy situation.

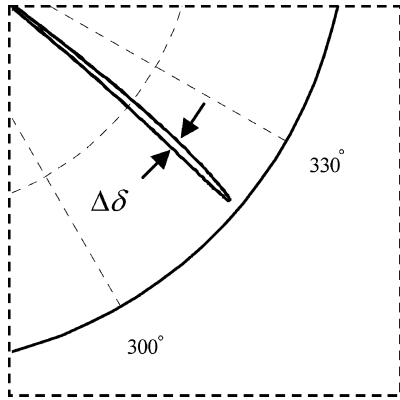


Fig. 9. Enlarged dotted-frame portion of Fig. 7, showing swing angle,  $\Delta\delta = \max(\Delta\delta(r) = \delta^{\max} - \delta^{\min})$ , in case of a 12 turns (5%) fault, (shorted through 1- $\Omega$  resistor.)

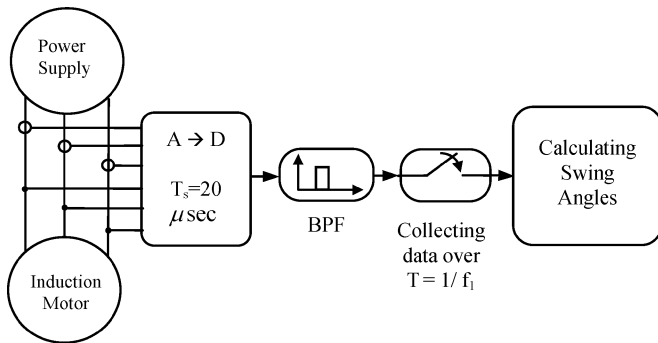


Fig. 10. Functional block diagram of the swing angle calculation for interturn fault diagnostics.

over the duration of a power cycle,  $T = 1/f_1$ , the angle,  $\delta(t)$ , where  $0 < \delta(t) < 2\pi$  rad, is calculated by (2). Then, the swing angle,  $\Delta\delta$ , is obtained by calculating the maximum spread of  $\Delta\delta(r) = \delta^{\max} - \delta^{\min}$  in a polar plot diagram; see Figs. 8 and 9. Thus, for each power cycle, a single value for the swing angle,  $\Delta\delta$ , is obtained. The results of the on-line interturn fault detection over five seconds for the case studies of the 5-hp and the 2-hp induction motors are shown in Figs. 11 and 12, respectively. As one can see in Figs. 11 and 12, if the circulating current,  $I_f$  (see Fig. 5) exceeds the value of line current,  $I_L$ , an interturn fault can be easily detected using the swing angle index.

At the same conditions, the peak values of an on-line trace of the negative sequence component of the line currents, which were obtained for each cycle, are shown over five seconds for the 5-hp and 2-hp motors in Figs. 13 and 14, respectively. Although the calculated negative sequence current component in test (b) and test (c) of Fig. 13 are very close during some periods of time, as shown with the oval-shaped dotted lines in this figure, the negative sequence of the line currents can still be considered as a reliable diagnostic tool in the 5-hp motor case. However, this is not the case for the 2-hp induction motor. As one can see in Fig. 14, it is almost absolutely impossible to detect interturn faults for the 2-hp motor using the negative sequence index because of the closeness or “bunching-up” nature of the traces. This is because of the fact that the rewind 2-hp mo-

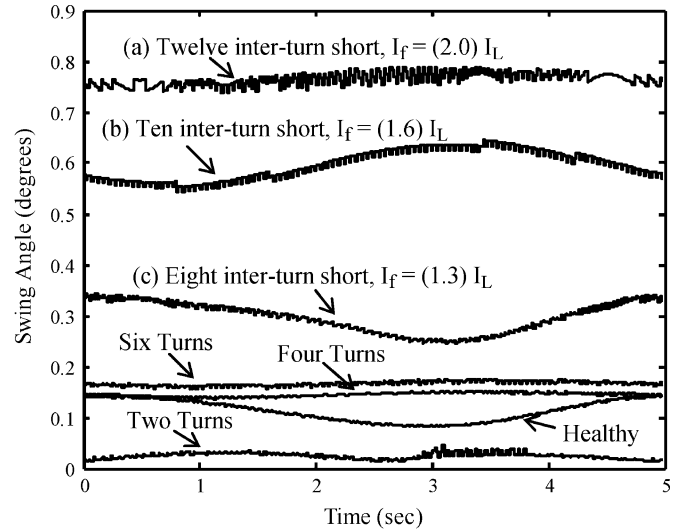


Fig. 11. Experimentally obtained swing angle,  $\Delta\delta$ , in degrees versus time in seconds for the 5-hp induction motor under healthy as well as two, four, six, eight, ten, and twelve turns fault through a one-ohm resistor.

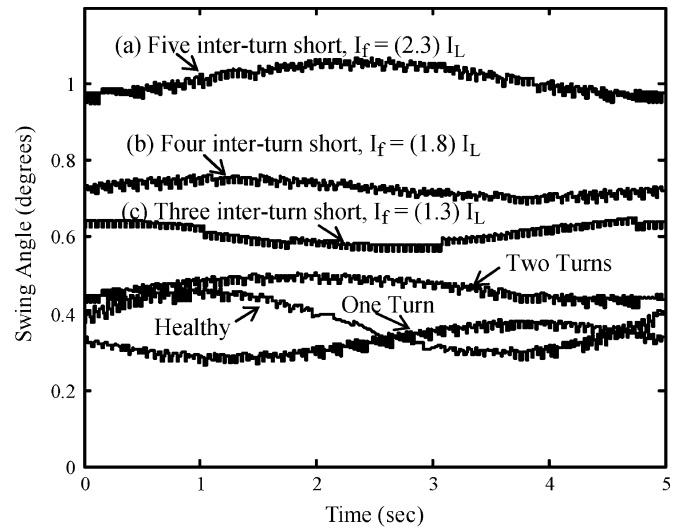


Fig. 12. Experimentally obtained swing angle,  $\Delta\delta$ , in degrees versus time in seconds for the 2-hp induction motor under healthy and one through five turns fault through a 0.8- $\Omega$  resistor.

tor had an inherent manufacturing degree of unbalance due to the manufacturing (or construction) imperfection resulting from the random winding installation process and the layout of the winding taps.

The average values of the swing angle,  $\Delta\delta$ , over the period of time shown in Figs. 11 and 12 and the negative sequence components of the line currents,  $I_n$ , the positive sequence components of the line currents,  $I_p$ , and terminal line to line voltages,  $V_n$ , calculated based on the peak values of the current and voltage phasors at fundamental frequency [3], as well as the motor terminal negative sequence impedance,  $z_n = V_n/(\sqrt{3}I_n)$  [3], [7] are given in Tables II and III for the case studies shown in Figs. 11–14. Moreover, Table IV demonstrates that the swing

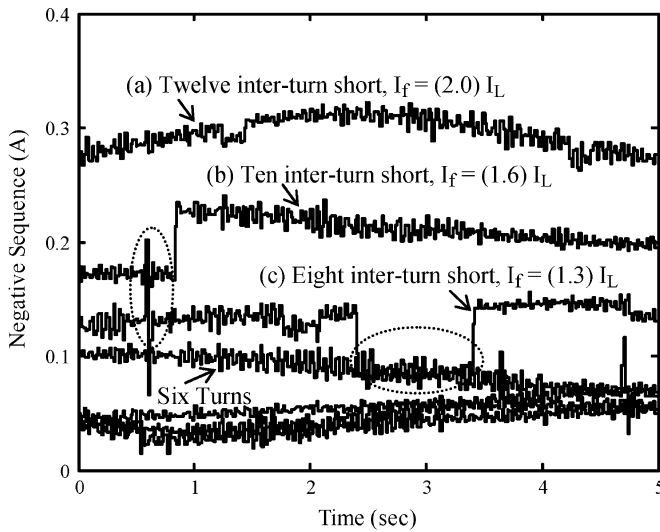


Fig. 13. Experimentally obtained peak negative sequence component of line currents  $I_n$  in amperes versus time in seconds for the 5-hp induction motor under healthy as well as two, four, six, eight, ten, and twelve turns fault through a 1- $\Omega$  resistor.

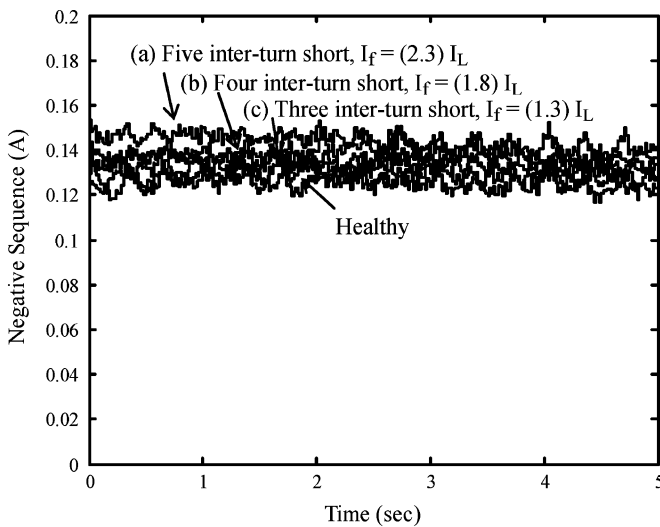


Fig. 14. Experimentally obtained peak negative sequence component of line currents  $I_n$  in amperes versus time in seconds for the 2-hp induction motor under healthy and one through five turns fault through a 0.8- $\Omega$  resistor.

angle as a function of the percentage of the circulating current versus the line current. It can be concluded that the swing angle index is a robust and reliable fault signature for interturn fault detection purposes, while the negative sequence components of motor terminal currents and impedances in the case of the 2-hp motor led to ambiguities.

Here, a question comes to mind: “What is the difference between the 2-hp and the 5-hp induction motors, which leads to ambiguities regarding the use of the negative sequence components approach in detecting the fault in the 2-hp motor?” This query is addressed in the next section.

## V. ANALYSIS AND DISCUSSION OF RESULTS

In this investigation a 2-hp and a 5-hp set of induction motors were examined under interturn short circuit faults. In order to

TABLE II  
COMPARISON BETWEEN AVERAGE VALUES MEASURED OVER FIVE SECONDS FOR THE SWING ANGLE IN DEGREES AND NEGATIVE SEQUENCE COMPONENTS AT 60 HZ, SINUSOIDAL EXCITATION—AT CONSTANT LOAD 30-nm, 5-hp, 6-POLE INDUCTION MOTOR

| ST (%) | $\Delta\delta^\circ$ | $I_n$ (A) | $V_n$ (V) | $z_n$ ( $\Omega$ ) | $I_p$ (A) | $I_f$ (A) |
|--------|----------------------|-----------|-----------|--------------------|-----------|-----------|
| 0.00   | 0.1449               | 0.0541    | 1.1237    | 12.1763            | 9.2669    | 0.00      |
| 0.83   | 0.0252               | 0.0408    | 1.1765    | 18.0377            | 9.2507    | 3.09      |
| 1.66   | 0.1252               | 0.0495    | 1.1765    | 18.0377            | 9.2534    | 6.18      |
| 2.50   | 0.1668               | 0.0874    | 1.2863    | 8.9228             | 9.2753    | 9.28      |
| 3.33   | 0.2973               | 0.1261    | 1.1204    | 5.2595             | 9.2763    | 12.37     |
| 4.16   | 0.5960               | 0.2053    | 1.3123    | 3.7518             | 9.1899    | 15.47     |
| 5.00   | 0.7652               | 0.2955    | 1.4401    | 2.8384             | 9.2436    | 18.56     |

TABLE III  
COMPARISON BETWEEN AVERAGE VALUES MEASURED OVER FIVE SECONDS FOR THE SWING ANGLE IN DEGREES AND NEGATIVE SEQUENCE COMPONENTS AT 60 HZ, SINUSOIDAL EXCITATION—AT CONSTANT SPEED 3510-r/min, 2-hp, 2-POLE INDUCTION MOTOR

| ST (%) | $\Delta\delta^\circ$ | $I_n$ (A) | $V_n$ (V) | $z_n$ ( $\Omega$ ) | $I_p$ (A) | $I_f$ (A) |
|--------|----------------------|-----------|-----------|--------------------|-----------|-----------|
| 0.00   | 0.3742               | 0.1363    | 3.2882    | 13.9372            | 3.7162    | 0.00      |
| 0.46   | 0.3282               | 0.1403    | 1.9624    | 8.2904             | 3.7960    | 1.73      |
| 0.93   | 0.4676               | 0.1382    | 1.3821    | 5.8050             | 3.7040    | 3.57      |
| 1.39   | 0.6082               | 0.1265    | 2.8478    | 13.0041            | 3.7289    | 5.21      |
| 1.85   | 0.7273               | 0.1342    | 3.0026    | 13.0375            | 3.7278    | 6.94      |
| 2.31   | 1.0147               | 0.1295    | 2.1435    | 9.6430             | 3.7163    | 8.68      |

TABLE IV  
COMPARISON BETWEEN THE 2-hp AND 5-hp INDUCTION MOTORS AVERAGE VALUES OF THE SWING ANGLE IN DEGREES VERSUS THE PERCENTAGE OF SHORTED TURNS AND THE SHORT CIRCUIT CIRCULATING LOOP CURRENT

| 5-hp Induction Motor |             |             |                      | 2-hp Induction Motor |             |             |                      |
|----------------------|-------------|-------------|----------------------|----------------------|-------------|-------------|----------------------|
| Shorted Turns        | ST (%)      | $I_f/I_L$   | $\Delta\delta^\circ$ | Shorted Turns        | ST (%)      | $I_f/I_L$   | $\Delta\delta^\circ$ |
| Healthy              | 0.00        | 0.00        | 0.144                | Healthy              | 0.00        | 0.00        | 0.374                |
| Two                  | 0.83        | 0.33        | 0.025                | One                  | 0.46        | 0.45        | 0.328                |
| Four                 | 1.66        | 0.66        | 0.125                | Two                  | 0.93        | 0.96        | 0.467                |
| Six                  | 2.50        | 0.99        | 0.166                | <b>Three</b>         | <b>1.39</b> | <b>1.39</b> | <b>0.608</b>         |
| <b>Eight</b>         | <b>3.33</b> | <b>1.33</b> | <b>0.297</b>         | <b>Four</b>          | <b>1.85</b> | <b>1.86</b> | <b>0.727</b>         |
| <b>Ten</b>           | <b>4.16</b> | <b>1.68</b> | <b>0.596</b>         | <b>Five</b>          | <b>2.31</b> | <b>2.33</b> | <b>1.014</b>         |
| <b>Twelve</b>        | <b>5.00</b> | <b>2.00</b> | <b>0.765</b>         | ----                 | ----        | ----        | ----                 |

create such a fault, the short circuits are conducted through an external 1- $\Omega$  resistor for the 5-hp motor and a 0.8- $\Omega$  resistor for the 2-hp motor to emulate the beginning of the breakdown of insulation between turns. The test results of the 5-hp motor show that the interturn faults can be detected using the swing angle,  $\Delta\delta$ , as well as the  $I_n$  and  $z_n$  indices, if the circulating current exceeds the motor line current, as observed from Table II. However, the test results of the 2-hp motor show that only the swing angle,  $\Delta\delta$ , as the fault signature (index) enables one to clearly detect an interturn fault, again this is possible if the circulating current exceeds the motor line current, as observed from Table III. Here, the earlier question comes to the mind: “What is the difference between the 2-hp and the 5-hp induction motors, which leads to ambiguities regarding the use of negative

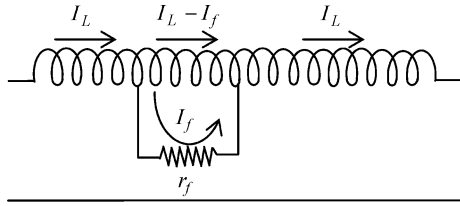


Fig. 15. Circuit schematic representation of a motor-phase with an interturn fault.

*sequence components approach in detecting the fault in the 2-hp motor?"* Before addressing this question, it has to be mentioned that the rewind 5-hp motor was built to a degree of perfection to render it a near perfectly balanced machine under healthy condition, while the 2-hp induction motor had a degree of construction imperfections. From Table II for the 5-hp motor, it can be observed that the negative sequence indices  $I_n$  and  $z_n$  can indicate an interturn fault only if the shorted turns (ST) exceed the threshold of 2.5 percent of the total number of turns per phase. From Table III, for the case of the 2-hp motor, it can be observed that the maximum number of shorted turns did not exceed 2.31% of the total number of turns per phase which is below the 2.5% threshold mentioned above, and the negative sequence indices could not indicate any interturn fault in this case. However, the corresponding short circuit circulating current  $I_f$  is more than twice the magnitude of the line current for the five turns fault (i.e., 2.31%) in the 2-hp motor; see Table III. In other words, the negative sequence component indices  $I_n$  and  $z_n$  are direct functions of the shorted turns (ST), and not a function of the circulating loop current ratio,  $I_f/I_L$ . However, the swing angle index,  $\Delta\delta$ , can indicate an interturn fault for both the 2-hp and 5-hp motors if the circulating current,  $I_f$ , exceeds the line current,  $I_L$ , ( $I_L \cong I_p$ ); see Table IV. Notice as it can be seen in Fig. 15, if the circulating short circuit current  $I_f$  increases beyond the line current  $I_L$  the shorted portion of the phase coil demagnetizes the rest of the impacted phase. This phenomenon can be observed by the negative sequence component of the motor currents if and only if it creates an asymmetry (nonequality) in the phase displacements or in the magnitudes of the three-phase current phasors. However, since such faults in the 2-hp motor are not significant enough to create these asymmetries and the 2-hp motor had a degree of construction imperfections, the negative sequence could not indicate such a fault. However, “*why could the swing angle index,  $\Delta\delta$ , indicate such a fault, regardless of the existence of the manufacturing imperfections?*” This is addressed next.

Based on the laboratory measurements, it was found that the peaks of the instantaneous line current  $I_L$  and the circulating current  $I_f$  do not occur at the same instance. Accordingly, the demagnetizing effect of the circulating current does not disturb the peak current of the impacted phase in a significant manner. However, the swing angle  $\Delta\delta$  is not based on only the peak values of the three phase currents. In other words, the swing angle is measured based on the *maximum thickness* of the polar plot ( $r, \delta$ ), see Fig. 16.

This means that asymmetries occurring at any point in the entire three phase current waveforms with respect to the voltage

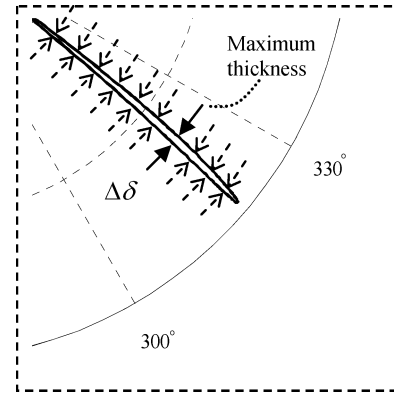


Fig. 16. Typical polar coordinate plot ( $r, \delta$ ) in case of an interturn fault, where  $\Delta\delta = \max(\Delta\delta(r)) = \delta^{\max} - \delta^{\min}$ .

waveforms  $\delta = \angle \vec{i}_s - \angle \vec{v}_s$  can be observed (or extracted) using the swing angle index,  $\Delta\delta$ ; see Fig. 16. This is the reason that the swing angle index can detect the interturn faults successfully for both the 2-hp and the 5-hp case study induction motors, regardless of the existence of any manufacturing imperfection effects, when the circulating current exceeds the motor line current; see Figs. 11 and 12.

## VI. CONCLUSION

A robust interturn fault diagnostic method based on the pendulous oscillation concept has been introduced and examined for the case studies of the 2-hp and the 5-hp induction motors. The experimental results have shown the strength and fidelity of this method, even in the presence of a degree of machine construction imperfections. It was also shown that the swing angle magnitude is a function of the ratio between the short circuit circulating current and the line (phase) current. Moreover, an interturn fault can be detected if the circulating current increases slightly beyond the phase current level even before the occurrence of higher levels of damaging circulating currents. Hence, the swing angle index enables one to detect stator interturn faults at an early stage to prevent further damage to the machine and involved systems. These concepts and findings have been verified experimentally in the results presented in this paper.

## APPENDIX

### INDUCTION MOTOR STATE-SPACE MODEL

In this Appendix, a simulation model of induction motors under interturn and broken bar fault conditions is presented in details based on the winding function method [10] and the line-to-line flux linkage state-space model [11]. This is done only for purposes of continuity and reproducibility of the work presented in this paper. The stator winding layout of phase-A and phase-B of a typical three-phase induction motor with the concentrated winding over a pole span are depicted in Fig. 17. Although the winding layout is assumed a concentrated winding, the results are valid for an induction motor with a lap winding. Here, the MMF profile of phase-A over 180 electrical degrees is

depicted in Fig. 18. In order to calculate the self inductance of phase-A, the total flux linkage of phase-A is obtained here as a summation of the individual flux linkage of each coil in a phase

$$\lambda_{ss} \Big|_{\substack{I_b=0, \\ I_c=0, \\ I_k=0, \\ k=1,2,\dots,N_{\text{bar}}}} = \sum_{j=1}^{N_{\text{coils}}} \lambda_{ssj} = \sum_{j=1}^{N_{\text{coils}}} N_j \phi_{ssj} \quad (\text{A1})$$

where,  $N_j$  is the number of turns per each coil and  $N_{\text{coils}}$  is the number of coils per pole per phase. In Figs. 17–19 just for the sake of graphical simplification,  $N_{\text{coils}} = 4$ . In (A1),  $\lambda_{ssj}$  is obtained by

$$\lambda_{ssj} = N_j \left( \frac{\mu_0 r l}{2g} \right) \left( \frac{\pi p}{N_{\text{slot}}} \right) \left( \sum_{k=1}^{N_{\text{coils}}} N_k \tau_{ck} \right) I_{\text{path}} \quad (\text{A2})$$

where  $j = 1, \dots, N_{\text{coils}}$ ,  $\tau_{ck}$  is the  $k$ th step-width in the MMF profile, see Fig. 18,  $\pi p / N_{\text{slot}}$  is the angular displacement between each two adjacent stator slots in electrical radians,  $N_{\text{slot}}$  is the total number of the stator slots,  $p$  is the number of poles,  $l$  is the rotor axial length,  $g$  is the effective air-gap height, and  $r$  is the motor radius at mid air-gap. Using (A1) and (A2) and after some algebraic manipulation, the stator self inductance can be expressed as follows:

$$L_{ss} = \left( \frac{\mu_0 r l}{2g} \right) \left( \frac{\pi p}{N_{\text{slot}}} \right) k_{se}^2 (N^T Q_{ss} N) \quad (\text{A3})$$

where  $k_{se} = 1$  for a parallel connection (low voltage) and  $k_{se} = 2$  for a series connection (high voltage), the vector  $N_{(N_{\text{coils}} \times 1)}$  and the matrix  $Q_{ss(N_{\text{coils}} \times N_{\text{coils}})}$  are defined as follows:

$$N = [N_1 \ N_2 \ \dots \ N_j \ \dots \ N_{\text{coils}}]^T \quad (\text{A4})$$

$$Q_{ss} = \begin{bmatrix} \tau_{c1} & \tau_{c2} & \dots & \tau_{cN_{\text{coils}}} \\ \tau_{c2} & \tau_{c2} & \dots & \tau_{cN_{\text{coils}}} \\ \dots & \dots & \ddots & \vdots \\ \tau_{cN_{\text{coils}}} & \tau_{cN_{\text{coils}}} & \dots & \tau_{cN_{\text{coils}}} \end{bmatrix}. \quad (\text{A5})$$

For instance, the vector  $N$  and the matrix  $Q_{ss}$  for the layout depicted in Fig. 18 are given as follows:

$$N = [N_1 \ N_2 \ N_3 \ N_4]^T$$

and

$$Q_{ss} = \begin{bmatrix} \tau_{c1} & \tau_{c2} & \tau_{c3} & \tau_{c4} \\ \tau_{c2} & \tau_{c2} & \tau_{c3} & \tau_{c4} \\ \tau_{c3} & \tau_{c3} & \tau_{c3} & \tau_{c4} \\ \tau_{c4} & \tau_{c4} & \tau_{c4} & \tau_{c4} \end{bmatrix}$$

where, for the winding layout shown in Figs. 17 and 18,  $\tau_{c1} = 11$ ,  $\tau_{c2} = 9$ ,  $\tau_{c3} = 7$ ,  $\tau_{c4} = 5$ .

If the same procedure is performed for the flux linkage of phase-A when phase-B is energized; see Fig. 19, one can write the following expression for the stator mutual inductance:

$$L_M = - \left( \frac{\mu_0 r l}{2g} \right) \left( \frac{\pi p}{N_{\text{slot}}} \right) k_{se}^2 (N^T Q_M N) \quad (\text{A6})$$

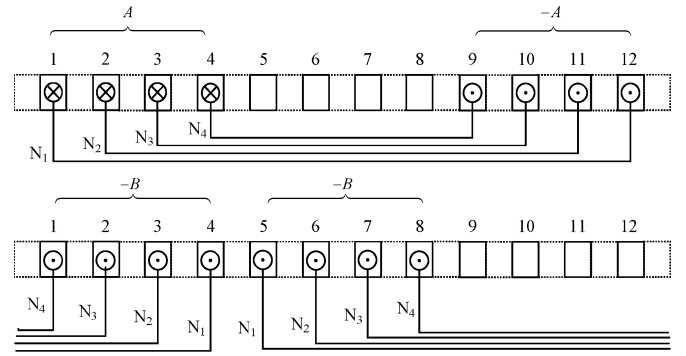


Fig. 17. Stator winding layout of phase-A and phase-B of a three-phase induction motor with a concentrated winding (over a pole span).

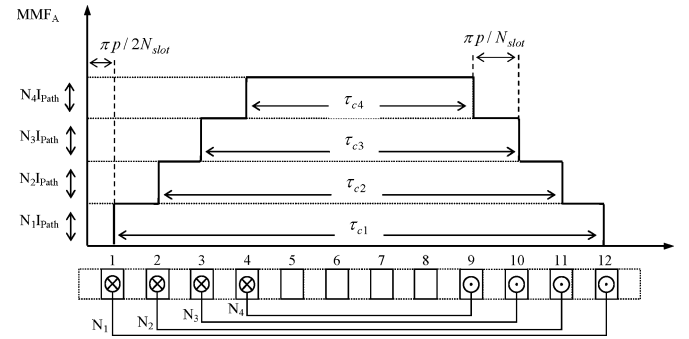


Fig. 18. MMF profile of phase-A of the stator winding over 180 electrical degrees (over a pole span).

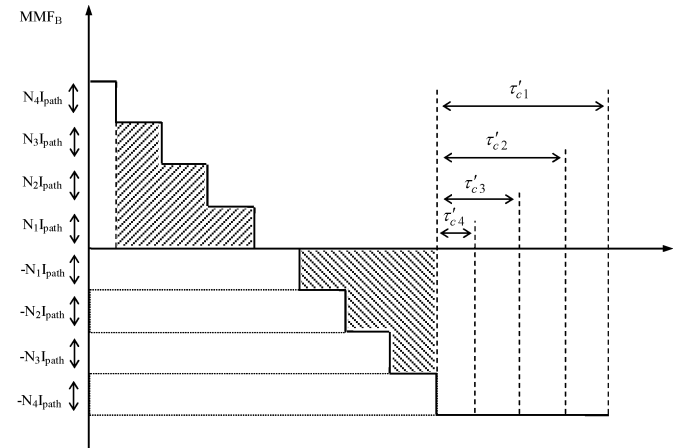


Fig. 19. MMF profile of phase-B of the stator winding over 180 electrical degrees (over a pole span).

where

$$Q_M = \begin{bmatrix} \tau'_{c1} & \tau'_{c1} & \tau'_{c1} & \tau'_{c1} \\ \tau'_{c1} & \tau'_{c1} & \tau'_{c1} & \tau'_{c2} \\ \tau'_{c1} & \tau'_{c1} & \tau'_{c2} & \tau'_{c3} \\ \tau'_{c1} & \tau'_{c2} & \tau'_{c3} & \tau'_{c4} \end{bmatrix}$$

for the layout shown in Fig. 17,  $\tau'_{c1} = 4$ ,  $\tau'_{c2} = 3$ ,  $\tau'_{c3} = 2$ ,  $\tau'_{c4} = 1$ ; see Fig. 19.

The mutual inductance between each phase of the stator windings and each loop of the rotor cage can be obtained using the Fourier series of the stator MMF waveform. To do this, one can

write the following expression for the stator MMF waveform of phase-A; see Fig. 18

$$\text{MMF}_A = \sum_{h=1,3,5,\dots}^{\infty} \left( \frac{4I_{\text{path}}}{h\pi} k_{\text{wh}} \sin\left(\frac{h\pi}{2}\right) \right) \times \sin(h\theta) \quad (\text{A7})$$

while  $k_{\text{wh}}$  is given by

$$k_{\text{wh}} = \sum_{j=1}^{N_{\text{coils}}} N_j \sin\left(\frac{\tau_{\text{cj}}\pi p}{2N_{\text{slot}}} h\right). \quad (\text{A8})$$

Meanwhile, one can write the following for the flux linkage of a healthy rotor loop:

$$\lambda_{s\ell 1} \Big|_{\substack{I_b=0, \\ I_c=0, \\ I_k=0, \\ k=1,2,\dots,N_{\text{bar}}}} = \int_{\theta_m - (\alpha/2)}^{\theta_m + (\alpha/2)} B_{s\ell 1} r l d\theta_m \quad (\text{A9})$$

where  $\theta = (p/2)\theta_m$ ,  $\alpha = 2\pi/N_{\text{bar}}$ ,  $N_{\text{bar}}$  is the total number of rotor bars, and  $B_{s\ell 1} = \mu_0 \text{MMF}_A / 2g$ . Accordingly, the mutual inductance between phase-A, and loop-one, assuming it is a healthy loop, is obtained as follows:

$$L_{s\ell 1} = \frac{4\mu_0 r l}{\pi g} \frac{2}{p} \sum_{h=1,3,5,\dots}^{\infty} \frac{k_{\text{se}} k_{\text{wh}}}{h^2} \sin\left(\frac{h\pi}{2}\right) \times \sin\left(\frac{h(p/2)\alpha}{2}\right) \sin(h\theta). \quad (\text{A10})$$

However, in general, the mutual inductance between each phase and each rotor loop with or without broken bars can be obtained from

$$L_{s\ell k}^{n_b} = \frac{4\mu_0 r l}{\pi g} \frac{2}{p} \sum_{h=1,3,5,\dots}^{\infty} \frac{k_{\text{se}} k_{\text{wh}}}{h^2} \sin\left(\frac{h\pi}{2}\right) \times \sin\left(\frac{h(n_b + 1)(p/2)\alpha}{2}\right) \times \sin(h(\theta - (p/2)\theta_{\ell 1\ell k})) \quad (\text{A11})$$

where  $n_b$  equals zero for a healthy loop and it equals to the number of adjacent broken bars for a defective loop, the subscript  $k$  indicates the  $k$  th loop of the rotor's squirrel-cage circuit and  $\theta_{\ell 1\ell k}$  is the angular displacement between loop-one and the  $k$ th loop in mechanical radians, and for phase-A  $\theta = \theta_a = (p/2) \int \omega_m(t) dt$ , for phase-B  $\theta = \theta_a - 2\pi/3$ , and

for phase-C  $\theta = \theta_a - 4\pi/3$ , where  $\omega_m(t)$  is the rotor angular velocity in mechanical radian per second obtained from the dynamics of the motor rotation.

In the case of interturn faults, the self inductance of an impacted phase, the mutual inductance between an defective phase and a healthy phase, and the mutual inductance between a rotor loop and an defective phase can be still calculated by (A3), (A6), and (A11) with slight adjustment in (A4) and (A8), assuming the number of shorted turns  $N_{\text{sc}}$  in a phase winding does not exceed the number of turns in the impacted coil. In this case, the only required adjustment is

$$N_j^{\text{new}} = N_j^{\text{healthy}} - N_{\text{sc}}. \quad (\text{A12})$$

Moreover, the number of stator phases (states) in a three-phase motor impacted by an interturn fault is increased to four, with the additional fourth phase representing the shorted portion of a phase winding. This fourth phase is mutually coupled to the original three phases and the rotor cage circuit. Assuming that an interturn fault occurs in phase-A, the self inductance of the additional phase can be approximated by the following:

$$L_{\text{sc}} = \left(\frac{\mu_0 r l}{g}\right) \left(\frac{\pi \tau_{\text{sc}}}{N_{\text{slot}}}\right) N_{\text{sc}}^2 \simeq \eta^2 L_{\text{ss}} \quad (\text{A13})$$

where  $\eta$  indicates the *effective* shorted turns ratio. Accordingly, the inductance matrix of the stator windings when an interturn fault occurs in phase-A can be obtained as shown in (A14) at the bottom of the page. Considering (A10) through (A12), assuming an interturn fault occurs in phase-A, the stator-rotor mutual inductance matrix is given by (A15) at the bottom of the page. Using the MMF profile of a rotor loop, the self inductance of healthy loops is given by [10]

$$L_{\ell\ell} = \frac{\lambda_{\ell\ell}}{I_{\text{loop}}} = \frac{\mu_0 r l}{g} \alpha \left(1 - \frac{\alpha}{2\pi}\right) \quad (\text{A16})$$

where  $\alpha = 2\pi/N_{\text{bar}}$  and  $N_{\text{bar}}$  is the total number of rotor bars. Meanwhile, using the rotor loop MMF waveform depicted in Fig. 20, the self inductance of a defective loop due to  $n_b$  adjacent broken bars is given by

$$L_{\ell\ell}^{n_b} = \frac{\lambda_{\ell\ell}}{I_{\text{loop}}} = \frac{\mu_0 r l}{g} (n_b + 1) \alpha \left(1 - \frac{\alpha(n_b + 1)}{2\pi}\right). \quad (\text{A17})$$

$$\mathbf{L}_{\text{s}} = \begin{bmatrix} (1-\eta)^2 L_{\text{ss}} + (1-\eta) L_{\text{sl}} & (1-\eta) L_{\text{M}} & (1-\eta) L_{\text{M}} & \eta(1-\eta) L_{\text{M}} \\ (1-\eta) L_{\text{M}} & L_{\text{ss}} + L_{\text{sl}} & L_{\text{M}} & \eta L_{\text{M}} \\ (1-\eta) L_{\text{M}} & L_{\text{M}} & L_{\text{ss}} + L_{\text{sl}} & \eta L_{\text{M}} \\ \eta(1-\eta) L_{\text{M}} & \eta L_{\text{M}} & \eta L_{\text{M}} & \eta^2 L_{\text{ss}} + \eta L_{\text{sl}} \end{bmatrix}. \quad (\text{A14})$$

$$\mathbf{L}_{\text{sr}} = \begin{bmatrix} (1-\eta) L_{a\ell 1} & (1-\eta) L_{a\ell 2} & \dots & (1-\eta) L_{a\ell k} & \dots & (1-\eta) L_{a\ell(N_{\text{bar}}-n_b)} \\ L_{b\ell 1} & L_{b\ell 2} & \dots & L_{b\ell k} & \dots & L_{b\ell(N_{\text{bar}}-n_b)} \\ L_{c\ell 1} & L_{c\ell 2} & \dots & L_{c\ell k} & \dots & L_{c\ell(N_{\text{bar}}-n_b)} \\ \eta L_{a\ell 1} & \eta L_{a\ell 1} & \dots & \eta L_{a\ell k} & \dots & \eta L_{a\ell(N_{\text{bar}}-n_b)} \end{bmatrix}. \quad (\text{A15})$$

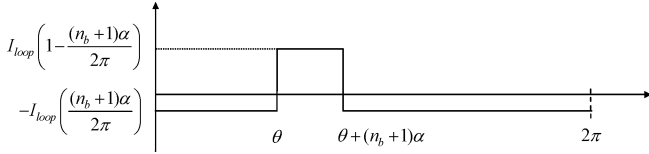


Fig. 20. MMF profile of a faulty loop of the rotor cage over 360 mechanical degrees.

Also, the mutual inductance between each two healthy loops is [10]

$$L_{\ell m} = (-1) \frac{\mu_0 r l}{g} \left( \frac{\alpha^2}{2\pi} \right). \quad (\text{A18})$$

Meanwhile, the mutual inductance between a defective loop and healthy loop is

$$L_{\ell m}^{n_b} = (-1) \frac{\mu_0 r l}{g} (n_b + 1) \left( \frac{\alpha^2}{2\pi} \right). \quad (\text{A19})$$

Accordingly, the rotor inductance matrix is obtained as shown in (A20) at the bottom of the page, where  $L_b$  and  $L_e$  are the leakage inductances of rotor-bar and rotor end-ring, respectively.

In a general case, the state-space representation of the model of stator windings can be expressed as follows:

$$v_{as} = r_{as} i_{as} + \frac{d\lambda_{as}}{dt} + v_n \quad (\text{A21})$$

$$v_{bs} = r_{bs} i_{bs} + \frac{d\lambda_{bs}}{dt} + v_n \quad (\text{A22})$$

$$v_{cs} = r_{cs} i_{cs} + \frac{d\lambda_{cs}}{dt} + v_n \quad (\text{A23})$$

where  $v_n$  indicates the instantaneous voltage at the neutral point of an assumed star-connection for the stator windings. Meanwhile, the state-space representation of the  $k$ th rotor healthy loop is given by

$$0 = 2(r_e + r_b) i_{\ell k} - r_b i_{\ell k-1} - r_b i_{\ell k+1} + \frac{d\lambda_{\ell k}}{dt} \quad (\text{A24})$$

where  $r_b$  and  $r_e$  are the rotor-bar and rotor-end-ring resistances, respectively. Meanwhile, for the  $m$ th loop with  $n_b$  adjacent broken bars the state-space representation is given by

$$0 = 2((n_b + 1)r_e + r_b) i_{\ell m} - r_b i_{\ell m-1} - r_b i_{\ell m+n_b+1} + \frac{d\lambda_{\ell m}}{dt}. \quad (\text{A25})$$

Now, in order to eliminate the unknown neutral voltage in the formulation and also have a stiff set of differential equations in the case of an interturn fault, (A21) through (A23) are reduced to only two differential equations as

$$v_{as} - v_{bs} = r_{as} i_{as} - r_{bs} i_{bs} + \frac{d\lambda_{ab}}{dt} \quad (\text{A26})$$

$$v_{bs} - v_{cs} = r_{bs} i_{bs} - r_{cs} i_{cs} + \frac{d\lambda_{bc}}{dt} \quad (\text{A27})$$

where the so-called line-to-line flux linkages,  $\lambda_{ab} = \lambda_{as} - \lambda_{bs}$  and  $\lambda_{bc} = \lambda_{bs} - \lambda_{cs}$ , are defined here as the state variables. Meanwhile, the state-space representation of the additional fourth phase, representing the shorted portion of phase-A, can be expressed by

$$0 = -r_f i_a + (r_{sc} + r_f) i_{sc} + \frac{d\lambda_{sc}}{dt} \quad (\text{A28})$$

where  $r_f$  is the external resistor in Fig. 15 ( $i_{sc} = i_a - i_f$ ), and  $r_{sc} = \eta r_{as}$ . It should be pointed out that, if  $r_f \gg \eta r_{as} = r_{sc}$ , (A28) can be expressed by the following algebraic equation:

$$0 = -r_f i_a + (r_{sc} + r_f) i_{sc} + \eta v_{as}. \quad (\text{A29})$$

Accordingly,  $\mathbf{L}_s$  in (A14) and  $\mathbf{L}_{sr}$  in (A15) are converted to 3-by-3 and 3-by- $(N_{\text{bar}} - n_b)$  matrices, respectively.

However, in general the state space representation of the electrical portion of the transient model can be represented by

$$(d/dt)\Lambda = (-\mathbf{R}\mathbf{L}^{-1})\Lambda + \mathbf{V} \quad (\text{A30})$$

where, in (A28),  $\Lambda$  is the vector of flux linkages,  $\mathbf{R}$ , and  $\mathbf{L}$  matrices are calculated using the formulations shown in (A31) at the bottom of the page, where  $\mathbf{R}_r$  is given by (A32) at the top of the next page. Meanwhile, matrix  $\mathbf{L}$  in (A30) is calculated through two steps in order to eliminate the third row and the third column of matrix  $\mathbf{L}_p$

$$\mathbf{L}_p = \begin{bmatrix} [\mathbf{L}_s]_{4 \times 4} & [\mathbf{L}_{sr}]_{4 \times (N_{\text{bar}} - n_b)} \\ [\mathbf{L}_{sr}^T]_{(N_{\text{bar}} - n_b) \times 4} & [\mathbf{L}_r]_{(N_{\text{bar}} - n_b) \times (N_{\text{bar}} - n_b)} \end{bmatrix}. \quad (\text{A33})$$

This is due to the fact that in (A28),  $V(1) = v_{ab} = v_a - v_b$ , and  $V(2) = v_{bc} = v_b - v_c$ . Meanwhile, the so-called "line-to-line" flux linkages are the stator windings state variables, namely  $\Lambda(1) = \lambda_{ab} = \lambda_a - \lambda_b$ , and  $\Lambda(2) = \lambda_{bc} = \lambda_b - \lambda_c$ . It should be noted that in case of using (A29) instead of (A28),  $\mathbf{L}_s$  and  $\mathbf{L}_{sr}$  will become a (3-by-3) and a (3-by- $(N_{\text{bar}} - n_b)$ ) matrices, respectively [12].

$$\mathbf{L}_r = \begin{bmatrix} L_{\ell\ell} + 2(L_b + L_e) & L_{\ell m} - L_b & \cdots & L_{\ell m}^{n_b} \\ L_{\ell m} - L_b & L_{\ell\ell} + 2(L_b + L_e) & \cdots & L_{\ell m}^{n_b} \\ \vdots & \vdots & \ddots & \vdots \\ L_{\ell m}^{n_b} & L_{\ell m}^{n_b} & \cdots & L_{\ell\ell} + 2(L_b + (n_b + 1)L_e) \end{bmatrix}. \quad (\text{A20})$$

$$\mathbf{R} = \begin{bmatrix} \begin{bmatrix} (1 - \eta)r_{as} & -r_{bs} & -r_f \\ r_{cs} & r_{bs} + r_{cs} & 0 \\ -r_f & 0 & r_f + \eta r_{as} \end{bmatrix} & [0]_{3 \times (N_{\text{bar}} - n_b)} \\ [0]_{(N_{\text{bar}} - n_b) \times 3} & [\mathbf{R}_r]_{(N_{\text{bar}} - n_b) \times (N_{\text{bar}} - n_b)} \end{bmatrix}. \quad (\text{A31})$$

$$\mathbf{R}_r = \begin{bmatrix} 2(r_b + r_e) & -r_b & 0 & \cdots & 0 & -r_b \\ -r_b & 2(r_b + r_e) & -r_b & 0 & \cdots & 0 \\ 0 & \ddots & \ddots & \ddots & \ddots & \vdots \\ \vdots & \ddots & \ddots & \ddots & \ddots & 0 \\ 0 & 0 & 0 & -r_b & 2(r_b + r_e) & -r_b \\ -r_b & 0 & 0 & 0 & -r_b & 2(r_b + (n_b + 1)r_e) \end{bmatrix}. \quad (\text{A32})$$

$$\mathbf{L}_{\text{aux}} = \begin{bmatrix} \mathbf{L}_p(1, [1, \dots, 4 + N_{\text{bar}} - n_b]) - \mathbf{L}_p(2, [1, \dots, 4 + N_{\text{bar}} - n_b]) \\ \mathbf{L}_p(2, [1, \dots, 4 + N_{\text{bar}} - n_b]) - \mathbf{L}_p(3, [1, \dots, 4 + N_{\text{bar}} - n_b]) \\ \mathbf{L}_p([4, \dots, 4 + N_{\text{bar}} + n_b], [1, \dots, 4 + N_{\text{bar}} - n_b]) \end{bmatrix}. \quad (\text{A34})$$

$$\mathbf{L} = \begin{bmatrix} \mathbf{L}_{\text{aux}}([1, \dots, 4 + N_{\text{bar}} - n_b], 1) - \mathbf{L}_{\text{aux}}([1, \dots, 4 + N_{\text{bar}} - n_b], 3) \\ \mathbf{L}_{\text{aux}}([1, \dots, 4 + N_{\text{bar}} - n_b], 2) - \mathbf{L}_{\text{aux}}([1, \dots, 4 + N_{\text{bar}} - n_b], 3) \\ \mathbf{L}_{\text{aux}}([1, \dots, 4 + N_{\text{bar}} + n_b], [4, \dots, 4 + N_{\text{bar}} - n_b]) \end{bmatrix}^T. \quad (\text{A35})$$

Step 1): Subtracting the third row of  $\mathbf{L}_p$  from the first and second row and eliminating the third row yields (A34) at the top of the page.

Step 2): Subtracting the third column of  $\mathbf{L}_{\text{aux}}$  from the first and second column and eliminating the third column yields (A35) at the top of the page. Thus, the entire set of  $\mathbf{R}$  and  $\mathbf{L}$  matrices for the stator and rotor have been defined.

In order to complete the state space model, the dynamics of the motor rotation are governed by the following equation based on Newton's law for rotational motion:

$$J \frac{d\omega_m(t)}{dt} = T_e(t) - T_m(t) \quad (\text{A36})$$

where  $\omega_m(t)$  is the rotor angular speed in mechanical rad/sec,  $J$  is the moment of inertia of the rotor-load system,  $T_m(t)$  is the mechanical load torque, and  $T_e(t)$  is the electromagnetic torque calculated by

$$T_e(t) = \left(\frac{p}{2}\right) I_s^T \frac{\partial \mathbf{L}_{\text{sr}}}{\partial \theta} I_r \quad (\text{A37})$$

where the matrix  $\partial \mathbf{L}_{\text{sr}} / \partial \theta$  is obtained from (A11) and (A15),  $I_s$  is the vector of stator winding currents, and  $I_r$  is the vector of the rotor loop currents.

#### ACKNOWLEDGMENT

The authors would like to thank Dr. P. Schmidt and Dr. F. Discenzo of Rockwell Corporation for providing the 5-hp test motors and access to their lab facilities.

The authors also would like to thank R. Bartos, S. Dellinger, and Dr. D. Ionel of A. O. Smith Corporation for providing the 2-hp test motor and access to their lab facilities.

#### REFERENCES

- [1] A. H. Bonnett and G. C. Soukup, "Cause and analysis of stator and rotor failures in three-phase squirrel-cage induction motors," *IEEE Trans. Ind. Appl.*, vol. 28, no. 4, pp. 921–937, Jul./Aug. 1992.
- [2] S. Williamson and K. Mirzozian, "Analysis of cage induction motors with stator winding faults," *IEEE Trans. Power App. Syst.*, vol. PAS-104, pp. 1838–1842, Jul. 1985.

- [3] C. F. Wagner and R. D. Evans, *Symmetrical Components*. New York: McGraw-Hill, 1961.
- [4] G. B. Kliman, W. J. Premerlani, R. A. Koegl, and D. Hoeweler, "A new approach to on-line turn fault detection in ac motors," in *Conf. Rec. Proc. IEEE-IAS Annu. Meeting*, vol. 1, 1996, pp. 687–693.
- [5] J. L. Kohler, J. Sottile, and F. C. Trutt, "Alternative for assessing the electrical integrity of induction motors," *IEEE Trans. Ind. Appl.*, vol. 28, no. 5, pp. 1109–1117, Sep./Oct. 1992.
- [6] S. B. Lee, R. M. Tallam, and T. G. Habetler, "A robust, on-line turn-fault detection technique for induction machines based on monitoring the sequence component impedance matrix," *IEEE Trans. Power Electron.*, vol. 18, no. 3, pp. 865–872, May 2003.
- [7] J. Sottile and J. L. Kohler, "An on-line method to detect incipient failure of turn insulation in random-wound motors," *IEEE Trans. Ind. Appl.*, vol. 28, pp. 921–937, Jul./Aug. 1992.
- [8] B. Mirafzal and N. A. O. Demerdash, "Induction machine broken-bar fault diagnosis using the rotor magnetic field space vector orientation," *IEEE Trans. Ind. Appl.*, vol. 40, no. 2, pp. 534–542, Mar./Apr. 2004.
- [9] B. Mirafzal and N. A. O. Demerdash, "Effects of load Magnitude on diagnosing broken bar faults in induction motors using the pendulous oscillation of the rotor magnetic field orientation," *IEEE Trans. Ind. Appl.*, vol. 41, no. 3, pp. 771–783, May/June 2005.
- [10] H. A. Toliyat and T. A. Lipo, "Transient analysis of cage induction machines under stator, rotor bar and end ring faults," *IEEE Trans. Energy Convers.*, vol. 10, no. 2, pp. 241–247, Jun. 1995.
- [11] M. G. Solveson, B. Mirafzal, and N. A. O. Demerdash, "Soft started induction motor modeling and heating issues for different starting profiles using a flux linkage ABC-frame of reference," in *Conf. Rec. Proc. IEEE-IAS Annu. Meeting*, vol. 1, no. 4, 2004, pp. 18–25.
- [12] B. Mirafzal, "Incipient Fault Diagnosis in Squirrel-Cage Induction Motors," Ph.D. dissertation, Marquette Univ., Milwaukee, WI, Aug. 2005.
- [13] B. Mirafzal and N. A. O. Demerdash, "On innovative methods of induction motor interturn and broken-bar fault diagnostics," in *Conf. Rec. Proc. IEEE-JEMDC*, May 15–18, 2005.



**Behrooz Mirafzal** (S'01) received the B.Sc. degree from Isfahan University of Technology, Isfahan, Iran, in 1994, and the M.Sc. degree (with first class honors) from the University of Mazandaran, Mazandaran, Iran, in 1997, both in electrical engineering. He is currently working toward the Ph.D. degree in the Department of Electrical and Computer Engineering, Marquette University, Milwaukee, WI.

From 1997 to 2000, he was a Research Engineer as well as a Lecturer at several academic institutions in Isfahan. His research interests include

power electronic applications to electric machines and drives, fault diagnostics in electric machines and drives, as well as power systems dynamics and stability problems.

Mr. Mirafzal is a member of the Electric Machines Committee of the IEEE Industry Applications Society.



**Richard J. Povinelli** (S'85–M'87–SM'01) received the B.S. degree in electrical engineering and the B.A. degree in psychology from the University of Illinois, Champaign-Urbana, in 1987, the M.S. degree in computer and systems engineering from Rensselaer Polytechnic Institute, Troy, NY, in 1989, and the Ph.D. degree in electrical and computer engineering from Marquette University, Milwaukee, WI, in 1999.

From 1987 to 1990, he was a Software Engineer with General Electric Corporate Research and Development. From 1990 to 1994, he was with GE Medical Systems, where he served as a Program Manager and then as a Global Project Leader. From 1995 to 1998, he held the positions of Lecturer and adjunct Assistant Professor with the Department of Electrical and Computer Engineering, Marquette University, where since 1999, he has been an Assistant Professor. His research interests include data mining of time series, chaos and dynamical systems, computational intelligence, and financial engineering. He has over 40 publications in these areas.

Dr. Povinelli was named Young Engineer of the Year by the Engineers and Scientists of Milwaukee in 2003. He is a member of the Association for Computing Machinery, American Society of Engineering Education, Tau Beta Pi, Phi Beta Kappa, Sigma Xi, Eta Kappa Nu, Upsilon Pi Epsilon, and Golden Key.



**Nabeel A. O. Demerdash** (M'65–SM'74–F'90) received the B.Sc.E.E. degree (distinction with first class honors) from Cairo University, Cairo, Egypt, in 1964, and the M.S.E.E. and Ph.D. degrees from the University of Pittsburgh, Pittsburgh, PA, in 1967 and 1971, respectively.

From 1968 to 1972, he was a Development Engineer with the Large Rotating Apparatus Development Engineering Department, Westinghouse Electric Corporation, East Pittsburgh, PA. From 1972 to 1983, he held the positions of Assistant Professor, Associate

Professor, and Professor in the Department of Electrical Engineering, Virginia Polytechnic Institute and State University, Blacksburg, VA. From 1983 to 1994, he held the position of Professor in the Department of Electrical and Computer Engineering, Clarkson University, Potsdam, NY. Since 1994, he has been a Professor in the Department of Electrical and Computer Engineering, Marquette University, Milwaukee, WI, in which he served as Department Chair from 1994 to 1997. He is the author or coauthor of more than 100 papers published in various IEEE Transactions. His research interests include power electronic applications to electric machines and drives, electromechanical propulsion and actuation, computational electromagnetics in machines and drives, as well as fault diagnostics and modeling of harmonic effects in machine-power systems.

Dr. Demerdash is active in the Electric Machinery Committees of the IEEE Power Engineering Society (PES), and its various subcommittees, as well as the Electric Machines Committee of IAS, and is listed in the Distinguished Lecturer Program of the PES and the Distinguished Speaker Program of the IEEE Industrial Electronics Society. He is the winner of the 1999 IEEE Nikola Tesla Technical Field Award. He is also the winner of two 1994 Working Group Awards from both the PES and its Electric Machinery Committee and a winner of two 1993 Prize Paper Awards from both the PES and its Electric Machinery Committee. He is a Member of the American Society of Engineering Education, Sigma Xi, and the Electromagnetics Academy.